The Astrophysical Journal Letters, 893:L29 (9pp), 2020 April 20 https://doi.org/10.3847/2041-8213/ab8563

WASP-4 Is Accelerating toward the Earth

L. G. Bouma[1], J. N. Winn[1], A. W. Howard[2], S. B. Howell[3], H. Isaacson[4], H. Knutson[5], and R. A. Matson[6]

[1] Department of Astrophysical Sciences, Princeton University, 4 Ivy Lane, Princeton, NJ 08540, USA; luke@astro.princeton.edu

[2] Cahill Center for Astrophysics, California Institute of Technology, Pasadena, CA 91125, USA

[3] NASA Ames Research Center, Moffett Field, CA 94035, USA

[4] Astronomy Department, University of California, Berkeley, CA 94720, USA

[5] Division of Geological and Planetary Sciences, California Institute of Technology, Pasadena, CA 91125, USA

[6] U.S. Naval Observatory, Washington, DC 20392, USA

Received 2020 February 28; revised 2020 March 27; accepted 2020 March 30; published 2020 April 17

Abstract

The orbital period of the hot Jupiter WASP-4b appears to be decreasing at a rate of -8.64 ± 1.26 ms yr^{-1}, based on transit-timing measurements spanning 12 yr. Proposed explanations for the period change include tidal orbital decay, apsidal precession, and acceleration of the system along the line of sight. To investigate further, we performed new radial-velocity measurements and speckle imaging of WASP-4. The radial-velocity data show that the system is accelerating toward the Sun at a rate of -0.0422 ± 0.0028 m s^{-1} day^{-1}. The associated Doppler effect should cause the apparent period to shrink at a rate of -5.94 ± 0.39 ms yr^{-1}, comparable to the observed rate. Thus, the observed change in the transit period is mostly or entirely produced by the line-of-sight acceleration of the system. This acceleration is probably caused by a wide-orbiting companion of mass 10–300 $M_{\rm Jup}$ and orbital distance 10–100 au, based on the magnitude of the radial-velocity trend and the nondetection of any companion in the speckle images. We expect that the orbital periods of one out of three hot Jupiters will change at rates similar to WASP-4b, based on the hot-Jupiter companion statistics of Knutson et al. Continued radial-velocity monitoring of hot Jupiters is therefore essential to distinguish the effects of tidal orbital decay or apsidal precession from line-of-sight acceleration.

Unified Astronomy Thesaurus concepts: Exoplanet tides (497); Exoplanet dynamics (490); Radial velocity (1332); Transit timing variation method (1710)

Supporting material: machine-readable tables

1. Introduction

The orbits of most hot Jupiters are formally unstable to tidal decay (Counselman 1973; Hut 1980; Rasio et al. 1996; Levrard et al. 2009; Matsumura et al. 2010). It is not clear, though, whether the timescale for tidal orbital decay is shorter or longer than the timescale for main-sequence stellar evolution. This answer to this question depends on the uncertain rate at which friction inside the star damps the tidal oscillations, which is ultimately what causes the orbit to shrink (as reviewed by Mazeh 2008 and Ogilvie 2014). Population studies of hot Jupiters—based on ages, rotation rates, orbital distances, and Galactic kinematics—have led to differing conclusions, with estimated lifetimes ranging from less than 1 Gyr to much longer than main-sequence lifetimes (see, e.g., Jackson et al. 2009; Teitler & Königl 2014; Collier Cameron & Jardine 2018; Penev et al. 2018; Hamer & Schlaufman 2019).

An empirical resolution might be possible through long-term timing of transits and occultations, seeking evidence for changes in the orbital period. For instance, long-term transit-timing and radial-velocity measurements for WASP-12b have revealed a secular decrease in the period at a rate of $\approx$30 ms yr^{-1}, which has been interpreted as the effect of tidal orbital decay (Maciejewski et al. 2016, 2018; Patra et al. 2017; Yee et al. 2020).

This study draws attention to a confounding factor that, while elementary, does not seem to have received the attention it deserves. The point is that observational programs aimed at identifying orbital decay in hot Jupiters through transit timing must be accompanied by concurrent long-term radial-velocity monitoring. The reason is that an apparent change in period can be produced by the Doppler effect associated with acceleration of the hot-Jupiter host star along the line of sight, such as the acceleration that might be produced by a massive, wide-orbiting companion. Massive outer companions to hot Jupiters are common. Bryan et al. (2016) calculated an occurrence rate of 70% $\pm$ 8% for outer companions to hot Jupiters with masses from 1 to 13 $M_{\rm Jup}$ and semimajor axes from 1 to 20 au. Therefore, we expect that many hot Jupiters will display secular trends in orbital period that are unrelated to tidal orbital decay. This possibility can be checked by performing long-term radial-velocity monitoring at a level sensitive enough to detect or rule out the relevant amplitude of acceleration.

The focus of this study is the hot Jupiter WASP-4b, which has an orbital period that appears to be decreasing by about 10 ms yr^{-1}. The period decrease was identified by Bouma et al. (2019, hereafter B19), who combined data from the NASA TESS mission (Ricker et al. 2015) and a decade of ground-based transit observations. Soon thereafter, Southworth et al. (2019) reported an additional 22 transit times and recalculated the period derivative to be $\dot{P} = -9.2 \pm 1.1$ ms yr^{-1}. A separate study by Baluev et al. (2019) reported on additional transit times, and pointed out that the period decrease was statistically significant only when analyzing the data with the highest precision.

To determine the origin of the period change, we acquired four additional radial-velocity measurements with the Keck I 10 m telescope and the High Resolution Echelle Spectrometer (HIRES; Vogt et al. 1994). In doing so, we extended the time baseline of HIRES measurements from 3 to 9 yr. The previously available HIRES data led to the marginal ($\approx 2\sigma$)

Table 1
WASP-4b Transit Times

t_{tra} (BJD_{TDB})	$\sigma_{t_{tra}}$ (days)	Epoch	Time Reference	Observation Reference
2454368.59279	0.00033	−1354	Hoyer et al. (2013)	Wilson et al. (2008)

Note. t_{tra} is the measured transit midtime, and $\sigma_{t_{tra}}$ is its 1σ uncertainty. "Time Reference" refers to the provenance of the timing measurement, which may differ from the "Observation Reference" in cases for which a homogeneous timing analysis was performed. The Hoyer et al. (2013) BJD_{TT} times are equal to BJD_{TDB} for our purposes (Urban & Seidelmann 2012).

(This table is available in its entirety in machine-readable form.)

Table 2
WASP-4b Radial Velocities

Time (BJD_{TDB})	RV ($m\ s^{-1}$)	σ_{RV} ($m\ s^{-1}$)	*S*-value	Instrument	Provenance
2454321.12345	42	0.42	0.42	HIRES	Knutson et al. (2014)

Note. *S*-values are reported only for the HIRES measurements.

(This table is available in its entirety in machine-readable form.)

detection of a radial-velocity trend (Knutson et al. 2014). Our new measurements reveal a line-of-sight acceleration of $\dot{\gamma} = -0.0422^{+0.0028}_{-0.0027}$ m s^{-1} day^{-1}. Through the Doppler effect,[7] this translates into an expected period decrease of −5.9 ms yr^{-1}, which is comparable to the period decrease that was measured from transit timing. We undertook high-resolution (speckle) imaging to search for evidence of a companion that could be responsible for the acceleration of WASP-4.

Section 2 of this Letter presents all of the available transit data as well as the new radial-velocity and speckle imaging observations. Section 3 describes our analysis of the data, and our interpretation that WASP-4 is being pulled around by a brown dwarf or low-mass star. Section 4 places this result within the context of orbital decay searches, and points out that line-of-sight accelerations will be a relatively common type of "false positive." Section 5 offers concluding remarks.

2. Observations

2.1. Transits

Table 1 lists the transit times we collected for our analysis. We included data from the peer-reviewed literature for which (i) the reported time was based on the data from a single transit (as opposed to fitting the data spanning multiple transits and assuming the period to be constant), (ii) the central transit time was allowed to be a free parameter, and (iii) the time system was documented clearly, in particular specifying whether barycentric or heliocentric corrections had been performed and whether leap seconds had been taken into account (TDB or UTC).

Most of these data are identical to the data presented by B19, which included observations by Wilson et al. (2008), Gillon et al. (2009), Winn et al. (2009), Hoyer et al. (2013), Dragomir et al. (2011), Sanchis-Ojeda et al. (2011), Nikolov et al. (2012), Ranjan et al. (2014), and Huitson et al. (2017). Twenty-two new times reported by Southworth et al. (2019) are included. These transits were observed from the 3.58 m New Technology Telescope and the Danish 1.54 m telescope at La Silla, Chile, and the South African Astronomical Observatory 1.0 m telescope. Additional timing measurements were also reported recently by Baluev et al. (2019), based on a homogeneous analysis of archival ground-based observations. We included their transit times from the TRAPPIST telescope (six transits), the El Sauce 36 cm (four transits), and Petrucci et al. (2013; two transits). For TRAPPIST and El Sauce, we verified with the original observers that the time stamps were amenable to the appropriate barycentric and leap-second corrections (M. Gillon & P. Evans 2020, private communication). We omitted the 14 remaining ETD[8] times from Baluev et al. due to ambiguity in whether leap-second corrections had been performed. We did not include in our analysis the four occultation times tabulated by B19, because of the large timing uncertainties and negligible statistical power.

2.2. Radial Velocities

We acquired four new radial-velocity measurements with Keck/HIRES. Our observations were performed using the standard setup and reduction techniques of the California Planet Survey (Howard et al. 2010). Previously, the HIRES data points spanned 2010–2013 (Knutson et al. 2014). Our new measurements triple the HIRES observing baseline to 9 yr.

The complete set of radial-velocity observations is given in Table 2. Along with the 2010–2019 HIRES observations are early measurements with two different spectrographs. Wilson et al. (2008) and Triaud et al. (2010) observed WASP-4 with the Swiss 1.2 m Euler Telescope and CORALIE Spectrograph; we adopted the radial-velocity values from the homogeneous analysis of the latter authors. We also included data from the High Accuracy Radial Velocity Planet Searcher (HARPS), reported by Pont et al. (2011) and Husnoo et al. (2012). While Triaud et al. (2010) also acquired HARPS data over three nights for Rossiter–McLaughlin observations, these data were reduced with a nonstandard pipeline making them ill suited for our study, and we did not include them.[9]

[7] While the apparent period change caused by a line-of-sight acceleration has been referred to as the "Rømer effect" (Yee et al. 2020), a simpler and probably better term is the Doppler effect. The Rømer effect refers to the *delay* in the reception of a signal due to a change in the time required for light to traverse the distance between the source and observer. The Doppler effect refers to the change in the apparent *rate* of a process due to changes in the relative motion of the source and observer, such as the rate of transits.

[8] http://var2.astro.cz/ETD

[9] This problem was fixed in principle by Trifonov et al. (2020), who performed a homogeneous re-reduction of the entire HARPS data archive. We found that the decision regarding whether to include or omit these points did not noticeably affect our results.

2.3. Speckle Imaging

Once we saw that the new HIRES observations implied a highly significant trend in the radial velocity, we sought independent evidence for a wide-orbiting companion by performing speckle imaging with the Zorro instrument on the Gemini South 8 m telescope (see Scott et al. 2018, and the instrument web pages[10]). Zorro is a dual-channel speckle interferometer employing narrowband filters centered at 562 and 832 nm.

We observed WASP-4 twice, on the night of September 11–12 with relatively poor seeing (1.″2) and also on the night of 2019 September 28–29. On each night, we acquired three sets of 1000 × 60 ms exposures. If a companion is present, the autocorrelation functions of these speckle images would reveal a characteristic interference pattern. This pattern is then used to determine the properties of the detected companion and produce a reconstructed image. Using the reconstructed speckle images, contrast curves are produced to determine the 5σ detection limits (see Howell et al. 2011). No companions were detected. The data from the second night, which had better seeing (0.″6), led to the most constraining limit. The 832 nm limits were the most useful, given that any faint companion would likely be redder than the host star. Therefore, we opted to use the 832 nm September 28–29 contrast limits in the analysis described below.

3. Analysis

3.1. Transits

We fitted two simple timing models to the transit-timing data. The first model assumes the period P to be constant:

$$t_{\rm tra}(E) = t_0 + PE, \quad (1)$$

where E is the integer specifying the number within the sequence of orbits spanned by the data, and t_0 is the transit time for the event designated $E = 0$. The second model assumes that the period changes at a steady rate:

$$t_{\rm tra}(E) = t_0 + PE + \frac{1}{2}\frac{dP}{dE}E^2. \quad (2)$$

The free parameters are the reference time t_0, the period at the reference time P, and the period derivative, $dP/dt = (1/P)\,dP/dE$. We defined the epoch numbers such that $E = 0$ is near the weighted average of the times of observed transits. This choice leads to a small covariance between the uncertainties in t_0 and P.

We fitted each model by assuming a Gaussian likelihood and sampling over the posterior probability distributions. The timing measurements, uncertainties, and provenances are given in Table 1. We sampled the posterior using the algorithm proposed by Goodman & Weare (2010) and implemented by Foreman-Mackey et al. (2013) in `emcee`. The prior for the quadratic model allowed the period derivative to be either positive or negative.

Figure 1 shows the observed transit times, minus the best-fitting constant-period model. The best-fitting constant-period model has 91 degrees of freedom, $\chi^2 = 276$, and $\chi^2_{\rm red} = 3.0$. The best-fitting quadratic model has 90 degrees of freedom, $\chi^2 = 183$, and $\chi^2_{\rm red} = 2.0$. The difference in the Bayesian information criteria (BIC) between the linear and quadratic and models is $\Delta{\rm BIC} = 89$, strongly favoring the quadratic model (Kass & Raftery 1995).

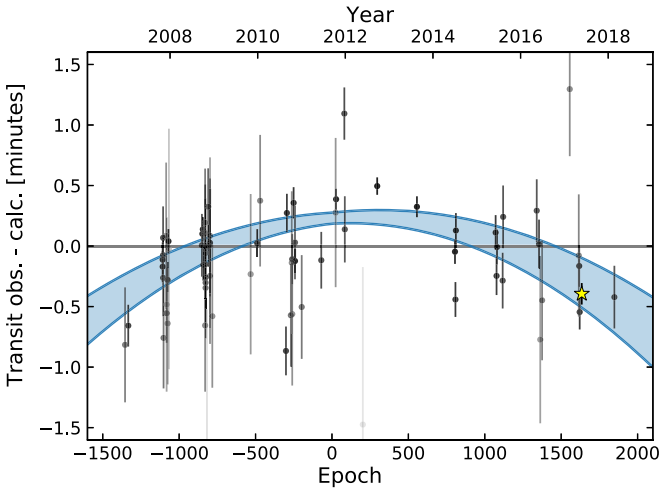

Figure 1. Timing residuals and best-fit models for WASP-4b. The vertical axis shows the observed transit times minus the calculated times, assuming a constant orbital period. More opaque points correspond to more precise data. The $\pm1\sigma$ uncertainties of the quadratic ephemeris are shown in blue. The yellow star represents the weighted average of 18 data points obtained with TESS. The TESS data were averaged here for display purposes only; our analysis used the 18 individual transit times.

From the high values of $\chi^2_{\rm red}$, we can surmise that neither model provides a satisfactory fit to the transit data; there must be some additional signal or noise. The earlier study by B19 found that the quadratic model for the (sparser) transit data gave $\chi^2_{\rm red} = 1.0$. The worsening of $\chi^2_{\rm red}$ could reflect underestimated statistical uncertainties in at least some of the newly reported transit times. It might also be due to systematic misunderstandings of the time systems in which the data were recorded, despite our best efforts to interpret the literature. In particular, mistaken leap-second corrections can introduce systematic errors of order one minute. Since we have no way of identifying which observations are affected by these issues, we opted to uniformly enlarge the uncertainties in the best-fitting parameters of each model by a factor of $(\chi^2_{\rm red})^{1/2}$. This was a factor of $\approx$1.73× for the linear model, and $\approx$1.41× for the quadratic model.

The resulting period derivative for the quadratic model is

$$\dot{P} = -(2.74 \pm 0.28) \times 10^{-10} = -8.64 \pm 1.26\ {\rm ms\ yr^{-1}}. \quad (3)$$

This agrees to within 1σ of the value reported by Southworth et al. (2019) ($\dot{P} = -9.2 \pm 1.1$ ms yr^{-1}). It is 2.3σ larger than the rate of period decrease reported by B19 (-12.6 ± 1.2 ms yr^{-1}), presumably because of the new data from Southworth et al. and Baluev et al. The other best-fitting model parameters are reported in Table 3.

3.2. Radial Velocities

Our initial model for the radial-velocity data was a circular orbit plus instrument offsets, "jitter" values (explained below), and a long-term linear trend (Fulton et al. 2018, `radvel`). We set Gaussian priors on the orbital period and time of inferior conjunction using the values from Table 4 of B19. We assumed the orbit to be circular based on previous studies that placed stringent upper limits on the eccentricity (Beerer et al. 2011;

[10] http://www.gemini.edu/sciops/instruments/alopeke-zorro/

Table 3
Best-fit Transit-timing Model Parameters

Parameter	Median Value (Unc.)[a]
Constant period	
t_0 (BJD_{TBD})	2456180.558712(+24)(−24)
P (days)	1.338231429(+26)(−26)
Constant period derivative	
t_0 (BJD_{TBD})	2456180.558872(+31)(−31)
P (days)	1.338231502(+24)(−24)
dP/dt	$-2.74(+40)(-40) \times 10^{-10}$

Note.
[a] The numbers in parenthesis give the 68% confidence interval for the final two digits, where appropriate. The intervals have been inflated by a factor of $(\chi^2_{red})^{1/2}$ due to excess scatter in the transit residuals (see Section 3.1).

Knutson et al. 2014; Bonomo et al. 2017). The free parameters were the orbital velocity semi-amplitude, the instrument zero-points, a "white noise" instrument jitter for each instrument added in quadrature to its uncertainties, and a linear ($\dot{v}_r$) acceleration term. (Without the linear trend, the model is a much poorer fit with $\Delta BIC = 73$.)

Figure 2 shows the results. In the best-fitting model, WASP-4 is accelerating along our line of sight at a rate

$$\dot{v}_r = \dot{\gamma} = -0.0422^{+0.0028}_{-0.0027}\ \mathrm{m\ s^{-1}\ day^{-1}}. \quad (4)$$

The other model parameters are listed in Table 4. Based on earlier data, $\dot{\gamma}$ was thought to be about five times smaller, and had marginal statistical significance (Knutson et al. 2014; Bouma et al. 2019).

Because of the Doppler effect, any line-of-sight acceleration should lead to a change in the observed orbital period:

$$\dot{P}_{RV} = \frac{\dot{v}_r P}{c}, \quad (5)$$

or in more convenient units,

$$\dot{P}_{RV} = 105.3\ \mathrm{ms\ yr^{-1}} \left(\frac{P}{\mathrm{day}}\right)\left(\frac{\dot{\gamma}}{\mathrm{m\ s^{-1}\ day^{-1}}}\right). \quad (6)$$

For WASP-4, this yields

$$\dot{P}_{RV} = -5.94 \pm 0.39\ \mathrm{ms\ yr^{-1}}. \quad (7)$$

Therefore, most of the period derivative that was detected through transit timing ($\dot{P} = -8.64 \pm 1.26\ \mathrm{ms\ yr^{-1}}$) can be accounted for by the Doppler effect. Given the evidence for unmodeled noise in both the transit-timing data and the radial-velocity data, it seems plausible that the Doppler effect can account for the entire observed period derivative.

An important consideration is whether the measured RV trend is truly due to acceleration or whether it is due to stellar activity. We investigate this by analyzing the Ca II H & K lines in the WASP-4 spectra, as quantified with the chromospheric S-index (Wright et al. 2004). We relied only on the HIRES velocities, which were the crucial source of information in the radial-velocity analysis. First, we subtracted the component of the best-fitting model representing the orbital motion induced by the planet. Then, following Bryan et al. (2016, 2019), we calculated the Spearman rank correlation coefficient between the S-index and the orbit-subtracted velocities. We found a correlation coefficient of 0.16. This correlation is not statistically significant; the corresponding p-value is 0.65. Furthermore, inspection of the S-index time series did not show secular or sinusoidal trends, as would be expected if we were observing a long-term magnetic activity cycle. The S-index values are included in Table 2. We conclude that there is no evidence that the linear trend is caused by stellar activity.

3.3. Constraints on Companion Masses and Semimajor Axes

Given a linear radial-velocity trend, we can place probabilistic constraints on the mass and semimajor axis of the additional body that is causing the trend. For a quick estimate of the minimum mass required to explain the linear trend in WASP-4, we turned to Feng et al. (2015). As they discussed, the scenario that yields the minimum companion mass for a system with a linear trend is a companion with $e \approx 0.5$ and $\omega = 90°$. Substituting $P \approx 1.25\tau$ and $K \approx 0.5\tau\dot{\gamma}$ into the mass function (e.g., Wright & Howard 2009) yields

$$M_{min} \approx 5.99\ M_{Jup} \left(\frac{\tau}{\mathrm{yr}}\right)^{4/3} \left|\frac{\dot{\gamma}}{\mathrm{m\ s^{-1}\ day^{-1}}}\right| \left(\frac{M_\star}{M_\odot}\right)^{2/3}, \quad (8)$$

where τ is the observing baseline. For WASP-4, this gives $M_{min} = 4.9\ M_{Jup}$. Higher masses are allowed for companions that orbit further from the star: at fixed $\dot{\gamma}$, $M_{comp} \propto a^2$ (Torres 1999; Liu et al. 2002).

High-resolution images can further limit the available parameter space by setting an upper limit on the companion brightness (and the corresponding mass) as a function of orbital distance. The procedure we used to combine constraints from both radial velocities and high-resolution imaging was developed by Wright et al. (2007), Crepp et al. (2012), Montet et al. (2014), Knutson et al. (2014), Bryan et al. (2016, 2019), and others.

Speckle Imaging Transformations. First, we converted the contrast curves obtained from speckle imaging (Figure 3) to upper limits on the companion mass as a function of projected separation. To do this, we followed Montet et al. (2014), and opted to employ the Baraffe et al. (2003) models for substellar-mass objects and the MIST isochrones for stellar-mass objects (Paxton et al. 2011, 2013, 2015; Choi et al. 2016; Dotter 2016). We assumed that the system age was 5 Gyr, at which point the companion would have fully contracted.

Due to the custom filters of the Zorro imager, and corresponding lack of synthetic photometry, we further assumed that all sources had blackbody spectra. While this is a simplification, we do not have ready access to the planetary and stellar atmosphere models needed for the consistent calculation with the `COND03` and `MESA` models. We adopted the effective temperatures and bolometric luminosities from the Baraffe et al. (2003) and MIST isochrones. Using these theoretical quantities and the empirically measured Zorro bandpasses, we calculated absolute magnitudes in the 562 and 832 nm Zorro bands for stellar and planetary mass companions. Applying the same calculation to WASP-4 itself using the effective temperature and bolometric luminosity from B19, we derived the transformation from contrast ratio to companion mass. The resulting limits derived if we assume maximal projected separations are shown with the dotted line in Figure 4. However, because the primary star is accelerating toward our line of sight, the companion could very well be near inferior conjunction. Our approach for incorporating the relevant projection effects is described in the following paragraphs.

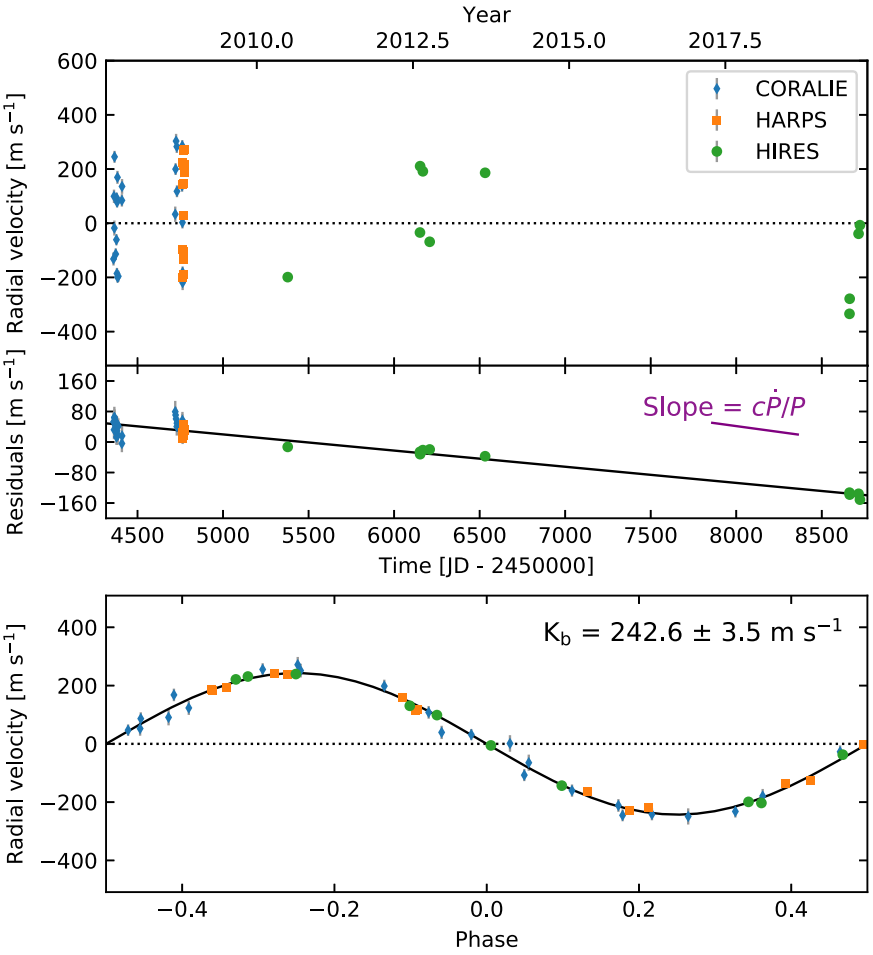

Figure 2. Radial velocities of WASP-4. Top: RV measurements, with best-fit instrument offsets added. Middle: residuals, after subtracting the best-fitting model for the variations induced by the planet WASP-4b. The black line is the linear trend inferred from the RV data. The purple line shows the slope that would be needed for the Doppler effect to explain the entire period decrease determined from transit timing. The four new RV measurements from this work increase the significance of the linear trend from $\approx 2\sigma$ to 15σ. Bottom: phased orbit of WASP-4b.

Table 4
Best-fit Radial-velocity Model Parameters

Parameter	Credible Interval	Maximum Likelihood	Units
Orbital Parameters			
P_b	$1.338231466 \pm 2.3e{-}08$	1.338231466	day
$T\mathrm{conj}_b$	$2455804.515752^{+2.5e-05}_{-2.4e-05}$	2455804.515752	$\mathrm{BJD_{TDB}}$
e_b	≡0.0	≡0.0	
ω_b	≡0.0	≡0.0	°
K_b	$242.6^{+3.6}_{-3.5}$	242.6	m s^{-1}
Other Parameters			
γ_{HIRES}	$36.4^{+5.8}_{-5.9}$	36.4	m s^{-1}
γ_{HARPS}	$-69.9^{+4.2}_{-4.1}$	−70.1	m s^{-1}
$\gamma_{\mathrm{CORALIE}}$	$-39.9^{+5.5}_{-5.2}$	−40.1	m s^{-1}
$\dot{\gamma}$	$-0.0422^{+0.0028}_{-0.0027}$	−0.0424	m s^{-1} day^{-1}
$\ddot{\gamma}$	≡0.0	≡0.0	
σ_{HIRES}	$10.8^{+3.7}_{-2.7}$	8.2	m s^{-1}
σ_{HARPS}	$13.0^{+3.7}_{-2.6}$	11.5	m s^{-1}
$\sigma_{\mathrm{CORALIE}}$	$13.8^{+6.6}_{-6.7}$	12.9	m s^{-1}

Note. Reference epoch for γ, $\dot{\gamma}$, $\ddot{\gamma}$: 2455470.

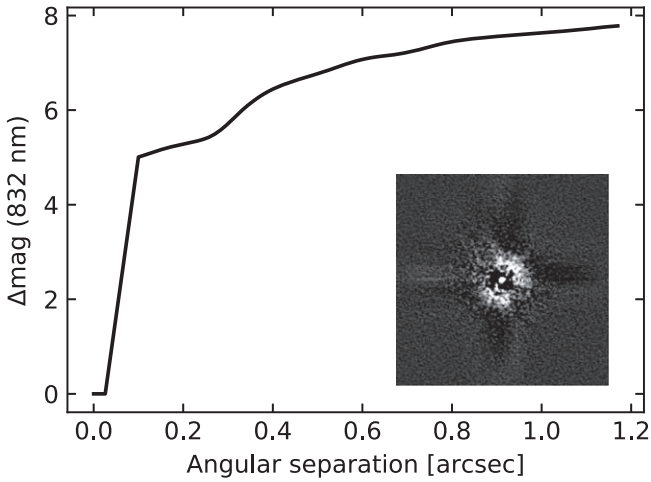

Figure 3. Zorro contrast limits derived from point-source injection-recovery experiments. Sources below the curve would have been detected. The inset shows the speckle image reconstructed from one thousand 60 ms frames in an 832 nm bandpass and acquired on 2019 September 28. The image scale is $2\farcs46 \times 2\farcs46$.

Combined Radial-velocity and Imaging Constraints. To derive constraints on possible companion masses and separations, we mostly followed the procedure of Bryan et al. (2019). We began by defining a 128 × 128 grid in true planetary mass and semimajor axis, over a logarithmic grid ranging from 1 to 900 M_{Jup} and 3 to 500 au. We then considered the possibility

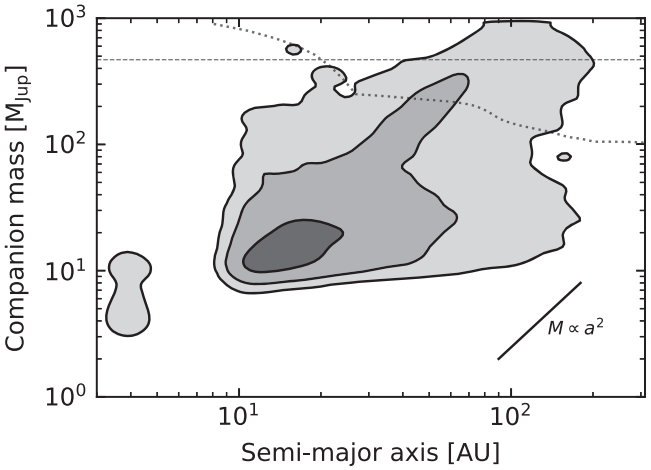

Figure 4. Masses and semimajor axes of companions that meet requirements of both the radial velocities and the speckle imaging. Contours show the joint radial-velocity and speckle imaging probability density with 1σ, 2σ, and 3σ significance. The dotted line shows the speckle imaging limits at maximal projected separation. Relevant projection effects were marginalized out when calculating the contours. The horizontal dashed line is the mass limit inferred from observations that WASP-4 is single lined, requiring any companion to contribute no more than one-tenth of the observed light. The black line shows the expected degeneracy between mass and semimajor axis.

that an additional companion in any particular cell could explain the observed linear trend.

For each grid cell, we simulated 512 hypothetical companions. We assigned each companion a mass and semimajor axis from log-uniform distributions within the boundaries of the grid cell. We drew the inclination from a uniform distribution in $\cos i$. For companion masses less than $10\,M_{\rm Jup}$, we drew the eccentricity from Kippin's (2013) long-period exoplanet Beta distribution ($a = 1.12$, $b = 3.09$). If the companion mass exceeded $10\,M_{\rm Jup}$, we drew the eccentricity from the power-law $p_e \propto e^{\eta}$ reported by Moe & Di Stefano (2017) in their Equation (17) ($\eta \approx 0.5$ for most orbital periods). The long-period exoplanet and long-period binary eccentricity distributions are quite different: the exoplanet distribution is "bottom-heavy," with eccentricities preferentially close to zero. The binary star distribution is "top-heavy," with a broad range of eccentricities extending close to unity (Moe & Di Stefano 2017; Price-Whelan et al. 2020). The choice of $10\,M_{\rm Jup}$ as the dividing line between these two regimes was based on the empirical study of Schlaufman (2018) on the distinction between giant planets and brown dwarfs. This value is also close to the $13\,M_{\rm Jup}$ deuterium-burning limit (e.g., Burrows et al. 1997).

The orbital properties of the inner hot Jupiter were assigned for each simulated system by sampling from from the radial-velocity posterior derived in Section 3.2. We subtracted the orbital component of the model from the observed RVs, leaving behind the RV residuals with a linear trend. Given (a_c, M_c, e_c) for each simulated outer companion, and the choice of instrument offsets and jitters, we performed a maximum likelihood fit for the time and argument of periastron of the outer simulated companion.

We then incorporated the speckle imaging limits in each simulated system as follows. After fitting for the time and argument of periastron, all the orbital parameters needed to find the projected separation at the time of observation are known. We assumed uniform sensitivity as a function of position angle, and therefore fixed the longitude of the ascending node to zero. We then calculated the projected separation using the parameterization given by Quirrenbach (2010). If a simulated companion's mass and projected separation put it above the 5σ contrast curve, we assumed it would have been detected. We multiplied the resulting $128 \times 128 \times 512$ cubes of radial-velocity and speckle imaging probabilities, and marginalized over the systems in each grid cell to derive a probability distribution in mass and semimajor axis. The contours in Figure 4 show the result: the companion responsible for the acceleration has a true mass of 10–300 $M_{\rm Jup}$ and an orbital distance of 10–100 au.

4. Discussion

4.1. Implications for WASP-4

The previously offered explanations for WASP-4b's decreasing orbital period included tidal orbital decay, apsidal precession, and the Doppler effect (Bouma et al. 2019). Our new radial-velocity measurements strongly indicate that the least exotic option—the Doppler effect—is the dominant physical process. Long-term transit-timing data show the orbital period to be decreasing by -8.64 ± 1.26 ms yr^{-1}. The long-term radial-velocity data show a trend that should lead to an apparent period derivative of -5.94 ± 0.39 ms yr^{-1} through the Doppler effect. Although these two measurements of the period derivative are discrepant by about 2σ, Occam's razor would suggest that the apparent decrease of WASP-4b's orbital period is caused solely by the line-of-sight acceleration. Detection of additional second-order effects will require more precise data, and a more significant discrepancy.

Based on the data, the companion causing the acceleration is probably either a brown dwarf or low-mass star with an orbital distance of 10–100 au (Figure 4). Given such a mass, this companion may have influenced the orbital evolution of the hot Jupiter orbiting WASP-4, as well as any other planets in the system. The fact that most hot Jupiters have similar massive outer companions (Knutson et al. 2014; Bryan et al. 2016) is compatible with some of the high-eccentricity formation theories for hot Jupiters (see Dawson & Johnson 2018). Further radial-velocity monitoring should eventually reveal the orbital parameters and minimum mass of WASP-4's massive outer companion.

Based on a priori expectations, if the outer companion lives within 100 au, then it seems more likely to be a brown dwarf than a low-mass star. The reason is that stellar companions within 100 au seem to be rare in systems with transiting planets, relative to field stars. This issue has been reviewed by Moe & Kratter (2019), who synthesized work by Wang et al. (2014, 2015), Ngo et al. (2015, 2016), Kraus et al. (2016), Matson et al. (2018), Ziegler et al. (2020), and others. A handful of systems with inner hot Jupiters and outer brown dwarfs within 100 au are known, for instance, CoRoT-20, HATS-59, WASP-53, and WASP-81 (Triaud et al. 2017; Rey et al. 2018; Sarkis et al. 2018). In contrast, from surveys by Knutson et al. (2014), Ngo et al. (2015), and Mugrauer (2019) we could find only one example of a system with an inner hot Jupiter and an outer low-mass star within 100 au: HAT-P-10 (Bakos et al. 2009). Overall, this body of literature indicates that the presence of a stellar-mass companion within 100 au of the host star could hinder the formation of planetary systems. If

Table 5
Predicted Hot-Jupiter Period Changes from Linear Radial-velocity Trends Reported by Knutson et al. (2014)

Planet	$\dot{\gamma}$ (m s^{-1} yr^{-1})	$+\sigma_{\dot{\gamma}}$ (m s^{-1} yr^{-1})	$-\sigma_{\dot{\gamma}}$ (m s^{-1} yr^{-1})	P (days)	$\dot{P}_{\rm RV}$ (ms yr^{-1})	$+\sigma_{\dot{P}\,\rm RV}$ (ms yr^{-1})	$-\sigma_{\dot{P}\,\rm RV}$ (ms yr^{-1})	Significant?
HAT-P-2 b	−0.0938	0.0067	0.0069	5.6335158	−55.62	3.97	4.09	1

Note. Orbital periods were retrieved from NASA's Exoplanet Archive. Additional comments regarding nonlinear trends and stellar activity are included in the MRT. (This table is available in its entirety in machine-readable form.)

true, then one would expect that the outer companion in WASP-4 would have the lowest mass allowed by the data.

4.2. How Many Other Hot Jupiters Are Accelerating toward Us?

We identified WASP-4b's decreasing orbital period as part of a search for tidal orbital decay. However, most hot Jupiters have companions outside of 5 au with super-Jovian masses (Knutson et al. 2014; Bryan et al. 2016). Line-of-sight accelerations (both positive and negative) should therefore be common in hot-Jupiter systems.

To evaluate the importance of these effects for future transit-timing analyses, we collected the linear radial-velocity trends reported by Knutson et al. (2014), and computed the expected orbital period derivatives $\dot{P}_{\rm RV} = \dot{v}_{\rm r} P/c$ for each system. The results are given in Table 5, and visualized for hot Jupiters with significant ($>3\sigma$) linear trends in Figure 5.

Including WASP-4b, 16 of 51 hot Jupiters surveyed by Knutson et al. (2014) show a nonzero radial-velocity trend. Therefore, around one in three hot Jupiters are expected to show period changes comparable to that of WASP-4 due to acceleration by outer companions. The sign of the accelerations should be random, with about half of them approaching and half of them receding. With a large enough sample of short-period hot Jupiters, one might be able to distinguish line-of-sight accelerations from tidal orbital decay by seeking evidence for a systematic tendency for the observed period to decrease, rather than increase.

4.3. At What Rate Is the Measurement Precision of dP/dt Increasing?

For hot Jupiters that have been monitored over baselines exceeding 10 yr, secular changes in their orbital periods are currently being constrained to a precision of $\lesssim$10 ms yr^{-1} (Patra et al. 2020; Wilkins et al. 2017; Maciejewski et al. 2018; Baluev et al. 2019; Petrucci et al. 2020). This is roughly commensurate with the level of signal many outer companions are expected to induce (Figure 5).

At what point in time will further detections of the Doppler effect become routine for hot Jupiters? More specifically, at what rate does the uncertainty in the quadratic term of Equation (2) scale with the observing baseline? This can be answered with a Fisher analysis of the model

$$t_{\rm tra} = a_0 + a_1 E + a_2 E^2, \tag{9}$$

where $a_0 \equiv t_0$, $a_1 \equiv P$, and $a_2 \equiv 0.5 \cdot {\rm d}P/{\rm d}E$. Following Gould (2003), one can show that if N transit-timing measurements are taken uniformly across a baseline of ΔE epochs with constant precision σ, then the uncertainty of the quadratic term

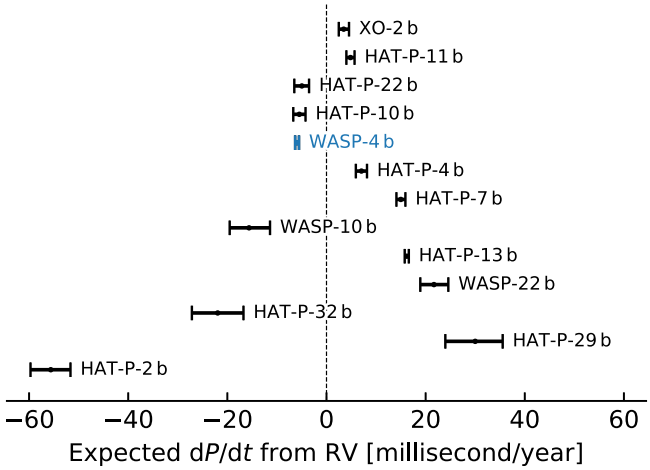

Figure 5. Predicted hot-Jupiter period changes from linear radial-velocity trends. Including WASP-4b, 16 of 51 hot Jupiters from Knutson et al. (2014) have shown long-term radial-velocity trends. HAT-P-11 is shown, though its signal is somewhat correlated with stellar activity (Yee et al. 2018). Three hot Jupiters are not shown because their radial-velocity curves are better described as quadratic trends in time: HAT-P-17, WASP-8, and WASP-34. Objects are ordered in the y dimension by the absolute value of dP/dt.

is given by

$$\sigma_{a_2} = 6\sqrt{5}\,\frac{\sigma}{N^{1/2}(\Delta E)^2} \propto (\Delta E)^{-5/2}. \tag{10}$$

This result implies that a doubled observing baseline yields an $\approx$5.7-fold improvement in precision on dP/dt. If regular observations continue from ground- and space-based observatories, period derivatives will be measured with precision exceeding 1 ms yr^{-1} within the coming decade.

5. Conclusions

From newly acquired radial-velocity measurements, we found that WASP-4 is accelerating toward the Earth at $\dot{\gamma} = -0.0422^{+0.0028}_{-0.0027}$ m s^{-1} day^{-1}. The corresponding Doppler effect predicts a period decrease $\dot{\gamma}P/c$ of -5.94 ± 0.39 ms yr^{-1}. The majority of the period decrease observed in transits ($\dot{P} = -8.64 \pm 1.26$ ms yr^{-1}) is therefore explained by the acceleration of the host star—leaving no evidence for tidal orbital decay or apsidal precession. A probabilistic analysis of the speckle imaging limits and the radial-velocity trend showed that the companion causing the acceleration is most likely a brown dwarf or low-mass star with a semimajor axis between 10 and 100 au.

Most hot Jupiters have outer companions with masses larger than Jupiter beyond 5 au (Knutson et al. 2014; Bryan et al. 2016). The accelerations and period changes induced by these outer companions will become an increasingly large nuisance in the hunt for tidal orbital decay as the observational baselines get longer. In particular, the precision with which the period

derivative can be measured from transits scales with the baseline duration to the 5/2 power (Section 4.3). Within a decade, many more hot Jupiters should show orbital period changes due to accelerations from their outer companions. To distinguish this effect from tidal decay, further long-term radial-velocity measurements of hot Jupiters are strongly encouraged.

Facilities: Gaia (Gaia Collaboration et al. 2016, 2018), Gemini:South (Zorro; Scott et al. 2018), Keck:I (HIRES; Vogt et al. 1994), Euler1.2m (CORALIE), ESO:3.6m (HARPS; Mayor et al. 2003), CTIO:1.0 m (Y4KCam), Danish 1.54 m Telescope, El Sauce:0.356 m, Elizabeth 1.0 m at SAAO, Euler1.2 m (EulerCam), Magellan:Baade (MagIC), Max Planck:2.2 m (GROND; Greiner et al. 2008) NTT, SOAR (SOI), TESS (Ricker et al. 2015), TRAPPIST (Jehin et al. 2011), VLT:Antu (FORS2).

Software: `astrobase` (Bhatti et al. 2018), `astropy` (Astropy Collaboration et al. 2018), `astroquery` (Ginsburg et al. 2018), `corner` (Foreman-Mackey 2016), `emcee` (Foreman-Mackey et al. 2013), `IPython` (Pérez & Granger 2007), `matplotlib` (Hunter 2007), `MESA` (Paxton et al. 2011, 2013, 2015) `numpy` (van der Walt 2011), `pandas` (McKinney 2010), `radvel` (Fulton et al. 2018), `scipy` (Jones et al. 2001).

ORCID iDs

L. G. Bouma https://orcid.org/0000-0002-0514-5538
J. N. Winn https://orcid.org/0000-0002-4265-047X
A. W. Howard https://orcid.org/0000-0001-8638-0320
S. B. Howell https://orcid.org/0000-0002-2532-2853
H. Isaacson https://orcid.org/0000-0002-0531-1073
R. A. Matson https://orcid.org/0000-0001-7233-7508

References

Astropy Collaboration, Price-Whelan, A. M., Sipőcz, B. M., et al. 2018, AJ, 156, 123
Bakos, G. Á., Pál, A., Torres, G., et al. 2009, ApJ, 696, 1950
Baluev, R. V., Sokov, E. N., Jones, H. R. A., et al. 2019, MNRAS, 490, 1294
Baraffe, I., Chabrier, G., Barman, T. S., Allard, F., & Hauschildt, P. H. 2003, A&A, 402, 701
Beerer, I. M., Knutson, H. A., Burrows, A., et al. 2011, ApJ, 727, 23
Bhatti, W., Bouma, L. G., Joshua, J., & Price-Whelan, A. 2018, Zenodo, doi:10.5281/zenodo.1469822
Bonomo, A. S., Desidera, S., Benatti, S., et al. 2017, A&A, 602, A107
Bouma, L. G., Winn, J. N., Baxter, C., et al. 2019, AJ, 157, 217
Bryan, M. L., Knutson, H. A., Howard, A. W., et al. 2016, ApJ, 821, 89
Bryan, M. L., Knutson, H. A., Lee, E. J., et al. 2019, AJ, 157, 52
Burrows, A., Marley, M., Hubbard, W. B., et al. 1997, ApJ, 491, 856
Choi, J., Dotter, A., Conroy, C., et al. 2016, ApJ, 823, 102
Collier Cameron, A., & Jardine, M. 2018, MNRAS, 476, 2542
Counselman, C. C. 1973, ApJ, 180, 307
Crepp, J. R., Johnson, J. A., Howard, A. W., et al. 2012, ApJ, 761, 39
Dawson, R. I., & Johnson, J. A. 2018, ARA&A, 56, 175
Dotter, A. 2016, ApJS, 222, 8
Dragomir, D., Kane, S. R., Pilyavsky, G., et al. 2011, AJ, 142, 115
Feng, Y. K., Wright, J. T., Nelson, B., et al. 2015, ApJ, 800, 22
Foreman-Mackey, D. 2016, JOSS, 1, 24
Foreman-Mackey, D., Hogg, D. W., Lang, D., & Goodman, J. 2013, PASP, 125, 306
Fulton, B. J., Petigura, E. A., Blunt, S., & Sinukoff, E. 2018, PASP, 130, 044504
Gaia Collaboration, Brown, A. G. A., Vallenari, A., et al. 2018, A&A, 616, A1
Gaia Collaboration, Prusti, T., de Bruijne, J. H. J., et al. 2016, A&A, 595, A1
Gillon, M., Smalley, B., Hebb, L., et al. 2009, A&A, 496, 259
Ginsburg, A., Sipocz, B., Madhura, P., et al. 2018, Zenodo, doi:10.5281/zenodo.1160627
Goodman, J., & Weare, J. 2010, Communications in Applied Mathematics and Computational Science, 5, 65
Gould, A. 2003, arXiv:astro-ph/0310577
Greiner, J., Bornemann, W., Clemens, C., et al. 2008, PASP, 120, 405
Hamer, J. H., & Schlaufman, K. C. 2019, AJ, 158, 190
Howard, A. W., Johnson, J. A., Marcy, G. W., et al. 2010, ApJ, 721, 1467
Howell, S. B., Everett, M. E., Sherry, W., Horch, E., & Ciardi, D. R. 2011, AJ, 142, 19
Hoyer, S., López-Morales, M., Rojo, P., et al. 2013, MNRAS, 434, 46
Huitson, C. M., Désert, J.-M., Bean, J. L., et al. 2017, AJ, 154, 95
Hunter, J. D. 2007, CSE, 9, 90
Husnoo, N., Pont, F., Mazeh, T., et al. 2012, MNRAS, 422, 3151
Hut, P. 1980, A&A, 92, 167
Jackson, B., Barnes, R., & Greenberg, R. 2009, ApJ, 698, 1357
Jehin, E., Gillon, M., Queloz, D., et al. 2011, Msngr, 145, 2
Jones, E., Oliphant, T., & Peterson, P. 2001, Open Source Scientific Tools for Python, https://www.scipy.org/
Kass, R. E., & Raftery, A. E. 1995, J. Am. Stat. Assoc., 90, 773
Kipping, D. M. 2013, MNRAS, 434, L51
Knutson, H. A., Fulton, B. J., Montet, B. T., et al. 2014, ApJ, 785, 126
Kraus, A. L., Ireland, M. J., Huber, D., Mann, A. W., & Dupuy, T. J. 2016, AJ, 152, 8
Levrard, B., Winisdoerffer, C., & Chabrier, G. 2009, ApJ, 692, L9
Liu, M. C., Fischer, D. A., Graham, J. R., et al. 2002, ApJ, 571, 519
Maciejewski, G., Dimitrov, D., Fernández, M., et al. 2016, A&A, 588, L6
Maciejewski, G., Fernández, M., Aceituno, F., et al. 2018, AcA, 68, 371
Matson, R. A., Howell, S. B., Horch, E. P., & Everett, M. E. 2018, AJ, 156, 31
Matsumura, S., Peale, S. J., & Rasio, F. A. 2010, ApJ, 725, 1995
Mayor, M., Pepe, F., Queloz, D., et al. 2003, Msngr, 114, 20
Mazeh, T. 2008, EAS, 29, 1
McKinney, W. 2010, in Proc. 9th Python in Science Conf., ed. S. van der Walt & J. Millman, 51
Moe, M., & Di Stefano, R. 2017, ApJS, 230, 15
Moe, M., & Kratter, K. M. 2019, arXiv:1912.01699
Montet, B. T., Crepp, J. R., Johnson, J. A., Howard, A. W., & Marcy, G. W. 2014, ApJ, 781, 28
Mugrauer, M. 2019, MNRAS, 490, 5088
Ngo, H., Knutson, H. A., Hinkley, S., et al. 2015, ApJ, 800, 138
Ngo, H., Knutson, H. A., Hinkley, S., et al. 2016, ApJ, 827, 8
Nikolov, N., Henning, T., Koppenhoefer, J., et al. 2012, A&A, 539, A159
Ogilvie, G. I. 2014, ARA&A, 52, 171
Patra, K., Winn, J., Holman, M., et al. 2020, AJ, 159, 150
Patra, K. C., Winn, J. N., Holman, M. J., et al. 2017, AJ, 154, 4
Paxton, B., Bildsten, L., Dotter, A., et al. 2011, ApJS, 192, 3
Paxton, B., Cantiello, M., Arras, P., et al. 2013, ApJS, 208, 4
Paxton, B., Marchant, P., Schwab, J., et al. 2015, ApJS, 220, 15
Penev, K., Bouma, L. G., Winn, J. N., & Hartman, J. D. 2018, AJ, 155, 165
Pérez, F., & Granger, B. E. 2007, CSE, 9, 21
Petrucci, R., Jofré, E., Gómez MaqueoChew, Y., et al. 2020, MNRAS, 491, 1243
Petrucci, R., Jofré, E., Schwartz, M., et al. 2013, ApJL, 779, L23
Pont, F., Husnoo, N., Mazeh, T., & Fabrycky, D. 2011, MNRAS, 414, 1278
Price-Whelan, A. M., Hogg, D. W., Rix, H.-W., et al. 2020, arXiv:2002.00014
Quirrenbach, A. 2010, in Astrometric Detection and Characterization of Exoplanets, ed. S. Seager (Tucson, AZ: Univ. Arizona Press), 157
Ranjan, S., Charbonneau, D., Désert, J.-M., et al. 2014, ApJ, 785, 148
Rasio, F. A., Tout, C. A., Lubow, S. H., & Livio, M. 1996, ApJ, 470, 1187
Rey, J., Bouchy, F., Stalport, M., et al. 2018, A&A, 619, A115
Ricker, G. R., Winn, J. N., Vanderspek, R., et al. 2015, JATIS, 1, 014003
Sanchis-Ojeda, R., Winn, J. N., Holman, M. J., et al. 2011, ApJ, 733, 127
Sarkis, P., Henning, T., Hartman, J. D., et al. 2018, AJ, 156, 216
Schlaufman, K. C. 2018, ApJ, 853, 37
Scott, N. J., Howell, S. B., Horch, E. P., & Everett, M. E. 2018, PASP, 130, 054502
Southworth, J., Dominik, M., Jø rgensen, U. G., et al. 2019, MNRAS, 490, 4230
Teitler, S., & Königl, A. 2014, ApJ, 786, 139
Torres, G. 1999, PASP, 111, 169
Triaud, A. H. M. J., Collier Cameron, A., Queloz, D., et al. 2010, A&A, 524, A25
Triaud, A. H. M. J., Neveu-VanMalle, M., Lendl, M., et al. 2017, MNRAS, 467, 1714
Trifonov, T., Tal-Or, L., Zechmeister, M., et al. 2020, A&A, in press
Urban, S., & Seidelmann, P. 2012, Explanatory Supplement to the Astronomical Almanac (Sausalito, CA: Univ. Science Books)
van der Walt, S., Colbert, S. C., & Varoquaux, G. 2011, CSE, 13, 22

Vogt, S. S., Allen, S. L., Bigelow, B. C., et al. 1994, Proc. SPIE, 2198, 362
Wang, J., Fischer, D. A., Horch, E. P., & Xie, J.-W. 2015, ApJ, 806, 248
Wang, J., Fischer, D. A., Xie, J.-W., & Ciardi, D. R. 2014, ApJ, 791, 111
Wilkins, A. N., Delrez, L., Barker, A. J., et al. 2017, ApJL, 836, L24
Wilson, D. M., Gillon, M., Hellier, C., et al. 2008, ApJL, 675, L113
Winn, J. N., Holman, M. J., Carter, J. A., et al. 2009, AJ, 137, 3826
Wright, J. T., & Howard, A. W. 2009, ApJS, 182, 205
Wright, J. T., Marcy, G. W., Butler, R. P., & Vogt, S. S. 2004, ApJS, 152, 261
Wright, J. T., Marcy, G. W., Fischer, D. A., et al. 2007, ApJ, 657, 533
Yee, S. W., Petigura, E. A., Fulton, B. J., et al. 2018, AJ, 155, 255
Yee, S. W., Winn, J. N., Knutson, H. A., et al. 2020, ApJL, 888, L5
Ziegler, C., Tokovinin, A., Briceño, C., et al. 2020, AJ, 159, 19